Current reversal leads to regime change in Amery Ice Shelf cavity in the twenty-first century

Jing Jin[1, a], Antony J. Payne[1, a], and Christopher Y. S. Bull[2]

[1]School of Geographical Sciences, University of Bristol, Bristol, UK
[2]Department of Geography and Environmental Sciences, Northumbria University, Newcastle Upon Tyne, UK
[a]now at: Department of Earth, Ocean and Ecological Sciences, University of Liverpool, Liverpool, UK

Correspondence: Jing Jin (Jing.Jin2@liverpool.ac.uk)

Abstract. The Amery Ice Shelf (AmIS), the third largest ice shelf in Antarctica, has experienced relatively low rates of basal melt during the past decades. However, it is unclear how AmIS melting will respond to a future warming climate. Here, we use a regional ocean model forced by different climate scenarios to investigate AmIS melting by 2100. The areally-averaged melt rate is projected to increase from 0.7 m·yr^{-1} to 8 m·yr^{-1} in the low-emission scenario or 17 m·yr^{-1} in the high-emission scenario in 2100. An abrupt increase in melt rate happens in the 2060s in both scenarios. The redistribution of local salinity (hence density) in front of AmIS forms a new geostrophic balance, leading to the reversal of local currents. This transforms AmIS from a cold cavity to a warm cavity, and results in the jump in ice shelf melting. While the projections suggest that AmIS is unlikely to experience instability in the coming century, the high melting draws our attention to the role of oceanic processes in basal mass loss of Antarctic ice shelves in climate change.

1 Introduction

The Amery Ice Shelf (AmIS) is a large ice shelf in Antarctica (Figure 1). It is fed by Lambert Glacier system which accounts for about 16% of the grounded ice in East Antarctica (Allison, 1979). AmIS has a deep grounding line reaching ∼2500m below sea surface (Galton-Fenzi et al., 2008; Yang et al., 2021; Chen et al., 2023), which makes it susceptible to ocean temperature changes in the deep ice shelf cavity, due to a low in-situ freezing point temperature (Galton-Fenzi et al., 2012; Wang et al., 2022).

Prydz Bay (PB) has a v-shaped coastline and constrains the AmIS (O'Brien et al., 2014). It is divided by Prydz Channel (PC)—a trough with the depth of ∼500 m at the shelf break and a deeper trough at the inner embayment named Amery Depression (AD) with bathymetry from 500-1000 m (Figure 1). The Fram Bank (FB) and the Four Ladies Bank (FLB) are located on the western and eastern side of AD, respectively, and exhibit dramatic differences of zonal topography (Figure 1). On the west of AD, the depth of FB rises sharply from ∼600 m to ∼200 m over a distance of ∼50 km. On the east of AD, FLB has a stepwise decrease from the depth of ∼200 m to ∼500m over a distance of ∼200 km (Liu et al., 2018).

Dense Shelf Water (DSW) and modified Circumpolar Deep Water (mCDW) are major water masses causing AmIS basal melting (Galton-Fenzi et al., 2012; Herraiz-Borreguero et al., 2015, 2016). DSW is dense and cold (slightly below the surface freezing point), which forms in coastal polynyas within PB during sea ice formation (Ohshima et al., 2013; Williams et al.,

25 2016; Portela et al., 2021). When DSW descends into the AmIS cavity, the temperature of DSW is higher than the in situ (pressure dependent) freezing point of seawater in the deepest cavity, which results in a basal melt rate of >30 m·yr^{-1} at the grounding line (Galton-Fenzi et al., 2012). The resulting meltwater, named Ice Shelf Water (ISW), upwells along the western ice shelf base. ISW, with a temperature of the in situ freezing point, can be supercooled when it is ascending and refreezing beneath the northwestern AmIS (Craven et al., 2009).

30 The cavity under AmIS is presently filled with relatively cold DSW of -2.2°C to -1.8°C (Craven et al., 2004; Herraiz-Borreguero et al., 2015). This results in relatively low basal melting along with basal refreezing beneath the northwestern AmIS (Depoorter et al., 2013; Rignot et al., 2013). Basal melt rates of AmIS have been stable during the past few decades (Adusumilli et al., 2020).

However, Southern Ocean temperatures are projected to increase in a warming climate (Fox-Kemper et al., 2021; Rintoul
35 et al., 2018). The previous studies predict the increased upwelling of mCDW onto the continental shelf of the AmIS sector, resulting in a shift of cavity regime and consequently an increase of basal melting (Naughten et al., 2018; Kusahara et al., 2023; Thomas et al., 2023; Mathiot and Jourdain, 2023). These studies provide insight into the drivers of warming on the continental shelf. For example, a freshening in PB increases vertical stratification, and induces the warming (Aoki et al., 2022; Thomas et al., 2023; Kusahara et al., 2023). Another mechanism is related to the poleward shift of westerly winds, which enhances
40 the upwelling of mCDW across the shelf break (Spence et al., 2017; Guo et al., 2019; Verfaillie et al., 2022). However, future changes in the links between the warming in PB and the warming in the AmIS ice shelf cavity, in other words, local oceanic currents/intrusive pathways of warm water, still lack investigation.

mCDW was thought to be absent in the AmIS cavity (Craven et al., 2004). However, it has been observed at the AmIS calving front entering the cavity during winter recently (Herraiz-Borreguero et al., 2015). Other hydrographical observations
45 and modelling studies have documented the presence of mCDW on the continental shelf in PB (Galton-Fenzi et al., 2012; Herraiz-Borreguero et al., 2015, 2016; Williams et al., 2016; Liu et al., 2017; Guo et al., 2022). The two main pathways of mCDW intruding beneath AmIS are:

1. A large cyclonic gyre encircles AD, known as Prydz Bay Gyre (PBG) (Smith et al., 1984; Nunes Vaz and Lennon, 1996; Heywood et al., 1999). mCDW upwells across the continental shelf, arriving at PB over FLB, and is transported by the eastern
50 branch of PBG toward AmIS (Galton-Fenzi et al., 2012; Herraiz-Borreguero et al., 2015; Williams et al., 2016; Liu et al., 2017). Some ISW exits the cavity and recirculates within PBG and returns beneath AmIS (Williams et al., 2016).

2. A narrow current flows between FLB and the East coast, named Prydz Bay Eastern Coastal Current (PBECC), which originates in the Antarctic Slope Current (ASC) (Liu et al., 2017, 2018). Due to the step-like deepened bathymetry over FLB, ASC is redirected shoreward to conserve potential vorticity, resulting in the formation of PBECC (Liu et al., 2018), bringing
55 mCDW to PB (Liu et al., 2017).

Previous studies have documented that a re-directed coastal current in front of Filchner-Ronne Ice Shelf (Hellmer et al., 2017; Naughten et al., 2021) and Ross Ice Shelf (Siahaan et al., 2022) drives a rapid warming of the ice shelf cavity in climate scenarios. The aim of this study is to determine whether the strength and direction of intrusive mCDW pathways in PB remain the same or change in response to future climate change, and how these changes affect the melt experienced by AmIS.
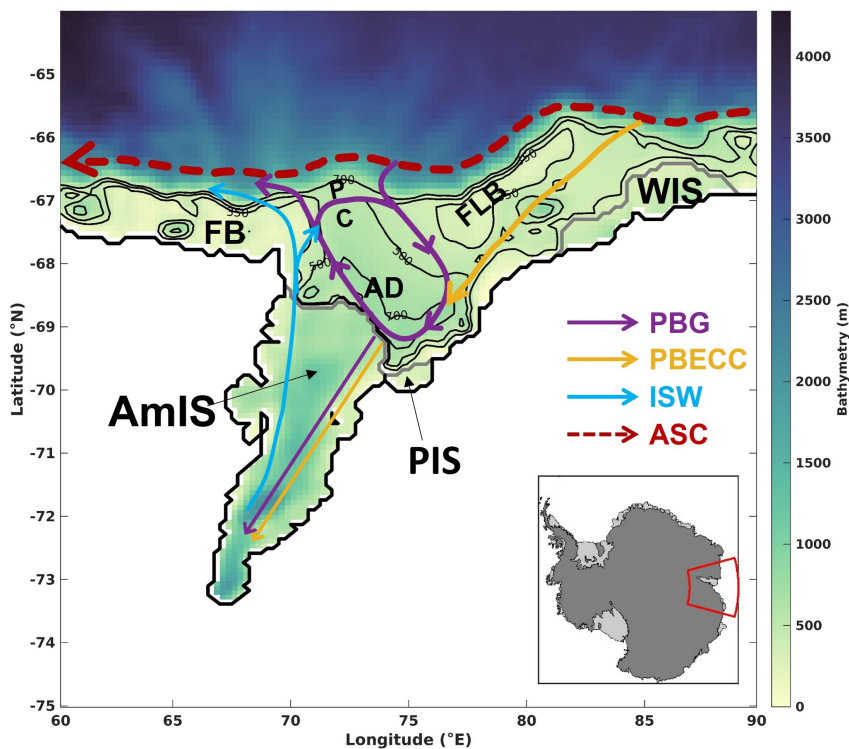
Figure 1. Model domain and schematic diagram of ocean circulation in Prydz Bay. The colour scale shows bathymetry (m). The thin black contours indicate bathymetry of 350 m, 500 m and 700 m. The thick black line represents the coastal line, and the thick grey lines show the ice shelf fronts. The thick red dashed arrow represents Antarctic Slope Current (ASC). Thick purple arrows show Prydz Bay Gyre (PBG). Thick yellow arrow indicates Prydz Bay Eastern Coastal Current (PBECC). Thin purple and yellow arrows in AmIS show modified Circumpolar Deep Water. Cyan arrows represent Ice Shelf Water (ISW). Geographical features are labelled as follows: AmIS: Amery Ice Shelf, PIS: Publications Ice Shelf WIS: West Ice Shelf, PC: Prydz Bay Channel, AD: Amery Depression, FLB: Four Ladies Bank, FB: Fram Bank. Inset: location of AmIS.

60   This paper is structured as follows: Section 2 describes our regional model configuration, model forcing and experiments; Section 3.1 presents projections of AmIS basal melting and temperature on the continental shelf; Section 3.2 proposes a mechanism driving the increase in AmIS basal melting; and Section 4 presents conclusions and discusses the limits and implications of this work.

2   Models and Methods

2.1   Regional model configuration

65

The regional NEMO configuration used to study Amery Ice Shelf-Prydz Bay (hereafter AME025) is summarised below.

The configuration includes the physical ocean engine OPA (Gurvan et al., 2017), a sea-ice model LIM3 (Rousset et al., 2015) and an open ice-shelf cavity (Mathiot et al., 2017). The model domain extends $30°$ in longitude (60-90°E) and $10°$ in latitude (65-75°S) with nominal $0.25°$ horizontal resolution with grid spacing increasing from $\sim$7 km to $\sim$12 km with increasing distance from the South Pole. A 75-level z^* vertical coordinate with a partial cell scheme is used in this work. It is a non-linear free surface application allowing for variations of volume according to the vertical resolution, and can adjust at top and bottom cells to represent bathymetry more realistically. The thicknesses of grid cells range from 1 m at the surface to 200 m at about 6000 m. Following Global Ocean version 7 (GO7) provided by Storkey et al. (2018), and bathymetry is derived from ETOPO1 data set (Amante and Eakins, 2009) with GEBCO giving modifications in coastal regions (IOC et al., 2003). Bathymetry under the ice shelf is derived from IBSCO (Arndt et al., 2013) and ice shelf draft is taken from BEDMAP2 (Fretwell et al., 2013).

The schemes and parameter values used in parameterisations are primarily based on GO7 (Storkey et al., 2018), but the values of lateral diffusivity and viscosity have been changed for our specific study, and some physical schemes, such as the slip condition for the lateral boundary, from other modelling studies (Mathiot et al., 2017; Jourdain et al., 2017; Bull et al., 2021) are taken into account as well. A 55-term polynomial approximation of the Thermodynamic Equation of Seawater (TEOS-10, IOC et al. 2010) is used in our configuration (Roquet et al., 2015). A vector-form formulation of the momentum advection is applied. The vorticity term is computed using conserving potential entropy and horizontal kinetic energy (Arakawa and Lamb, 1981). Lateral diffusion of tracers is evaluated using Laplacian isoneutral mixing with a coefficient of 135 m^2·s^{-1}. Lateral diffusion of momentum uses bi-Laplacian geopotential viscosity with a coefficient of -1.08$\times$10^{-10} m^4·s^{-1}. The vertical eddy viscosity and diffusivity coefficients are calculated from a Turbulent Kinetic Energy (TKE) scheme, with a background vertical eddy viscosity and vertical eddy diffusivity of 1.2$\times$10^{-4} m^2·s^{-1} and of 2$\times$10^{-6} m^2·s^{-1}, respectively. The enhanced vertical diffusion parameterization is implemented for tracer convective processes with a coefficient of 10 m^2·s^{-1}. The non-linear bottom friction parameterization is chosen, with a non-dimensional bottom drag coefficient of 2.5$\times$10^{-3}. The no-slip condition is implemented at the lateral momentum boundary.

Ice shelf thermodynamics are parameterised by the three-equation formulation with velocity dependent heat and salt exchange coefficients (Jenkins et al., 2010). The top boundary is set at 30 m below the ice shelf draft (or the first wet cell if the grid thickness is thicker than 30 m), and the top drag coefficient is set as 2.5$\times$10^{-3}. The heat and salt exchange coefficients are 1.4$\times$10^{-2} and 4$\times$10^{-4}, respectively. This implementation does not include external tidal forcing. The velocity of the tidal current at the top boundary is prescribed as 5 cm·s^{-1}.

The atmospheric surface boundary conditions and the oceanic lateral boundary conditions are derived from the UKESM1 outputs (Sellar et al., 2020).

2.2 UKESM1 forcing

We use climate projections made by the UK Earth System Model (UKESM1) as part of the CMIP6 exercise (Sellar et al., 2020). UKESM1 is based on the HadGEM3-GC3.1 physical climate model, with additional atmospheric chemistry, and marine and terrestrial biogeochemistry components (Sellar et al., 2020). The ocean model for UKESM1 is NEMO3.6, and it is based on Global Ocean version 6 (GO6) configuration (Storkey et al., 2018), with 1° horizontal resolution and 75 vertical levels.

Model outputs from the first ensemble member (r1i1p1f2) of UKESM1 have been assessed by previous studies (Beadling et al., 2020; Heuzé, 2021; Purich and England, 2021; Roach et al., 2020; Bracegirdle et al., 2020; Meehl et al., 2020; Forster et al., 2020). To briefly summarise the evaluations of the modelled Southern Ocean in historical simulations, UKESM1 has relatively small biases in upper (0-100 m) ocean temperature (Beadling et al., 2020, Figure 6, Figure S3) and salinity (Beadling

105 et al., 2020, Figure 6, Figure S4), and bottom temperature (Heuzé, 2021, Figure A3) and salinity (Heuzé, 2021, Figure A2) compared to other CMIP6 models. For the interior ocean, UKESM1 captures temperature and density structure across the continental shelf (Purich and England, 2021, Figure S2). It exhibits small cold (<-1°C) and fresh (<-0.15 psu) biases close to the shelf break along the 90°E longitudinal transect (Beadling et al., 2020, Figure S5) which is the easterly ocean boundary of the AME025 configuration. In addition, UKESM1 shows accuracy in representing the position and strength of westerly

110 jet over the Southern Ocean (Bracegirdle et al., 2020, Table 4). However, it is notable that UKESM1 has a higher climate sensitivity compared with other CMIP6 models (Forster et al., 2020, Figure 1; Meehl et al., 2020, Table 2), which might result in an unrealistically high surface warming (Forster et al., 2020). Additionally, UKESM1 overestimates Antarctic sea ice loss in summer (Beadling et al., 2020; Roach et al., 2020), which might cause a larger fresh bias at the ocean surface. Moreover, UKESM1 has a relatively coarse 1° grid which cannot present some oceanographical features close to the Antarctic margin.

115 Mathiot et al. (2011) suggest a minimum 0.5° nominal resolution to capture the ASC and local gyres on the continental shelf.

No external freshwater fluxes of surface runoff and ice sheet melting are used in the AME025 configuration. These freshwater fluxes implicitly enter our domain through the lateral ocean boundary conditions. The version of UKESM1 used in this study does not have an interactive ice sheet component. The ice sheet fluxes in UKESM1 are modelled in three parts (Sellar et al., 2020): (1) Surface runoff is simulated by the land surface model component of UKESM1; (2) As UKESM1 uses closed ice

120 shelf cavities, the meltwater flux from ice shelves is prescribed and spatially distributed between the depths of the calving front and the averaged grounding line (Mathiot et al., 2017); and (3) UKESM1 incorporated the iceberg flux through a Lagrangian iceberg model implemented in NEMO (Marsh et al., 2015). The freshwater flux of meltwater (45%) and iceberg calving (55%) is calibrated by the modelled pre-industrial surface mass balance of the Southern Hemisphere (Sellar et al., 2020).

2.3 Experimental design

125 Three experiments will be presented in this study: a historical simulation during 1976-2014 (Historical); a projection under SSP5-8.5 high emission scenario during 2015-2100; and a projection under SSP1-2.6 which is an optimistic emission scenario during 2015-2100.

Initial conditions consist of ocean temperature and salinity in January 1976 derived from GO7 (Storkey et al., 2018), which include an open cavity beneath AmIS. Atmospheric and oceanic forcing of our simulations are provided by the r1i1p1f2 ensem-

130 ble member of UKESM1 over the period of 1976-2100. The surface atmospheric forcing comprises daily variables, including near-surface air temperature at 2 m, specific humidity at 2 m, horizontal wind components at 10 m; surface downwelling longwave and shortwave radiation; and precipitation (rainfall and snowfall). It is applied through CORE bulk formulae (Large and Yeager, 2004). Note that surface runoff is not applied in the simulations. The lateral ocean boundary conditions consist
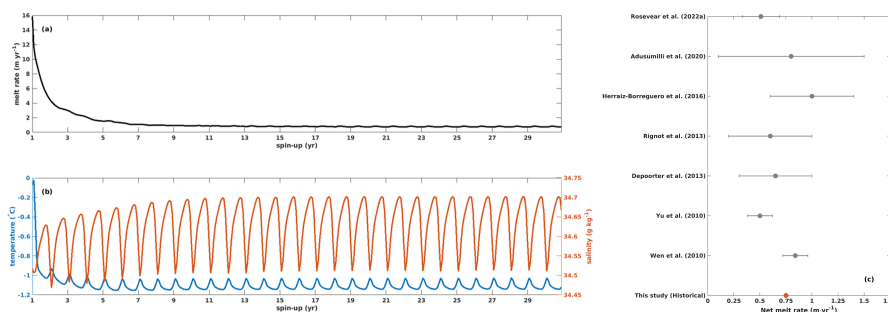
Figure 2. Time series of (a) area-averaged basal melting of AmIS ($m \cdot yr^{-1}$), (b) temperature ($^\circ$C, blue line and y-axis on the left) and salinity ($g \cdot kg^{-1}$, red line and y-axis on the right) in 30-year spin-up run. (c) Comparisons of AmIS melt rate among different studies. The grey dots represent the estimate of the AmIS melt rate and uncertainties from observational studies. The red dot shows the average of modelled AmIS melt rate from Historical simulation (1976-2014) in our study.

135 of monthly ocean and sea ice variables, including sea surface temperature, sea surface height; ocean temperature, salinity, barotropic and baroclinic velocity; sea ice fraction, sea ice thickness and snow thickness.

The model outputs are saved as monthly mean. Therefore, the processes shorter than one month are not considered in this study.

The initialisation process is carried out by repeatedly simulating the first year (which is 1976) until model drift becomes small. The time series of area-averaged melt rates of AmIS in the spin-up run shows that it achieves equilibrium after about 10
140 years (Figure 2a). The melt rate dramatically declines from $\sim$16 $m \cdot yr^{-1}$ in the first spin-up year to $\sim$1 $m \cdot yr^{-1}$ in year 9 and becomes stable afterwards. The averaged temperature and salinity in the entire domain exhibit similar behaviours (Figure 2b).

Comparisons between the modelled melt rate in the Historical experiment (1976-2014) and the observational melt rate found in other studies (Wen et al., 2010; Yu et al., 2010; Depoorter et al., 2013; Rignot et al., 2013; Herraiz-Borreguero et al., 2016; Adusumilli et al., 2020; Rosevear et al., 2022a) are shown in Figure 2c. The time-mean melt rate during 1976-2014 in our
145 study is 0.75 $m \cdot yr^{-1}$. This agrees with other estimates ranging from 0.5$\pm$0.12 to 1$\pm$0.4 (Figure 2c).

3 Results

3.1 The projected changes in the PB-AIS system by 2100

3.1.1 The increased basal melting

Figure 3 shows the time evolution of the area-averaged AmIS basal melting from 1976 to 2100. The melt rates fluctuate around
150 0.7 $m \cdot yr^{-1}$ until 2056, then abruptly jump to $\sim$13 $m \cdot yr^{-1}$ under SSP5-8.5 and $\sim$9 $m \cdot yr^{-1}$ under SSP1-2.6 in about 2066 (Figure 3a). The melt rate has a moderate increasing trend after 2066 and eventually reaches its peak at 16.8 $m \cdot yr^{-1}$ in 2100
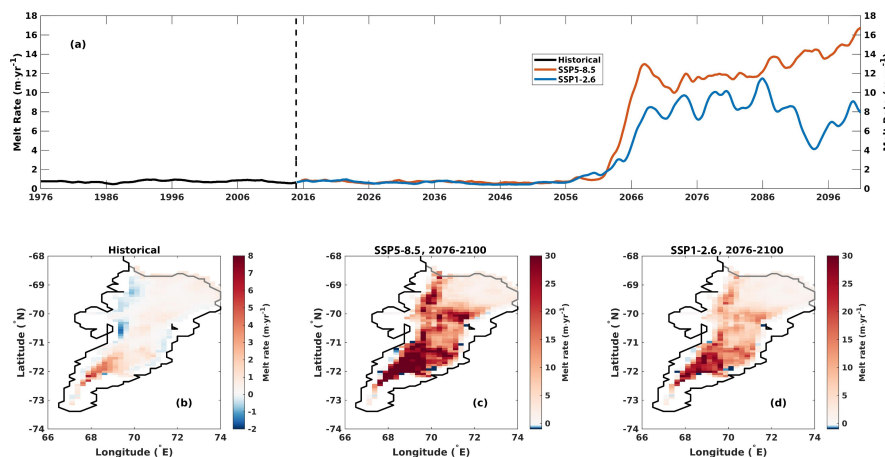
Figure 3. (a) Time series of the area-averaged melt rate ($m \cdot yr^{-1}$) from 1976 to 2100. A 12-month-running-average is applied. The dashed vertical line indicates the start of 2015. The time-averaged basal melting over the period of (b) 1976-2014 (Historical), (c) 2076-2100 under SSP5-8.5, (d) 2076-2100 under SSP1-2.6. The warm/cold colours represent melting/refreezing, respectively. Note the different colormap ranges. The colormap for (c) is saturated.

under SSP5-8.5, while it stays stable around $8\ m \cdot yr^{-1}$ after 2066 except for a decrease to $4\ m \cdot yr^{-1}$ in 2094 under SSP1-2.6 (Figure 3a).

Figure 3b-d shows the spatial distributions of the AmIS basal melting during the historical, and before and after the increase.
155 In general, after the increase in the 2060s the melting beneath AmIS strongly increases by multiple times and there is almost no refreezing. The time-averaged melt rates over 1976-2014 illustrate that a high melting of $\sim 6\ m \cdot yr^{-1}$ occurs near the grounding line and most of the ice shelf experiences melting smaller than $2\ m \cdot yr^{-1}$ (Figure 3b). The freezing mainly occurs under the northwestern ice shelf with the highest value of $\sim 1.6\ m \cdot yr^{-1}$ near 69.5°E, -70.5°N (Figure 3b). Smaller freezing rates (<0.2 $m \cdot yr^{-1}$) occur along the ice shelf edges (Figure 3b). This pattern fits the understanding of the buoyancy-driven meridional
160 overturning circulation, in which warm and dense inflows downwell in the eastern ice shelf cavity while cold and fresh outflows upwell in the western cavity. The time-averaged melt rates during 2075-2100 under SSP5-8.5 show that the melting occupies the entire ice shelf with the highest melt rates of $42\ m \cdot yr^{-1}$ near the grounding line (Figure 3c). Most of the areas experience melting between 15 and $35\ m \cdot yr^{-1}$ excluding the northeastern ice shelf which exhibits the relatively lower melting of ~ 5 $m \cdot yr^{-1}$ (Figure 3c).
165 The time-averaged melt rates over 2015-2055 under SSP1-2.6 (Figure 3d) have similar behaviour to those under SSP5-8.5 (Figure 3c). The spatial distributions of melt rates over 2075-2100 for SSP1-2.6 are similar to those for SSP5-8.5, but with a smaller melt rate of $\sim 30\ m \cdot yr^{-1}$ near the grounding line and 10-25 $m \cdot yr^{-1}$ over the central and the northwestern ice shelf (Figure 3d).

3.1.2 Warming on the continental shelf

170 Figure 4a shows the time series of temperature between 300 and 800 m on the continental shelf. The shelf break is generally defined at latitude of 67°S. The temperature under both SSP scenarios is steady before the late 2030s with the value of roughly -1.8 °C which is slightly above the surface freezing point (Figure 4a). It gradually increases by ∼2.4 °C to ∼0.6 °C in the late 2060s then increases to ∼0.8 °C in 2100 under SSP5-8.5 (Figure 4a). The temperature increases by 1.8 °C to 0 °C in the late 2060s and keeps steady until 2100 but with a decrease to ∼-0.9 °C in about 2094 under SSP1-2.6 (Figure 4a). The

175 temperature changes are similar to the melt rate changes (Figure 4a). However, the increase in temperature (in the 2030s) happens several decades prior to that in the melt rates (in the 2060s). The delayed increase in melting might suggest delayed processes connecting temperature and melting such as the passage of warm water into the cavity.

The spatial pattern of temperature before and after the increase in the 2060s is shown in Figure 4b-d. In general, after the increase, a warming occupies the entire domain, and the AmIS transforms from a cold cavity to a warm cavity. The time-depth-

180 averaged temperature in the open ocean in the Historical simulations decreases from ∼-0.5 °C near the northwestern boundary to ∼-1.9 °C near the calving front, and the steep gradients exist along the shelf break (Figure 4b). The temperature in the ice shelf cavity of AmIS increases from ∼-2.2 °C in the northern cavity to ∼-2 °C near the grounding line, and is also beneath -2 °C in the West Ice Shelf (WIS) cavity (Figure 4b). This indicates that the sub-ice shelf cavity is dominated by Dense Shelf Water (DSW).

185 In comparison with the Historical (1976-2014), the temperature under SSP5-8.5 is warmer as expected (Figure 4c). The warming is generally 0.5 °C over the northwestern open ocean, and increases to more than 1 °C over the northeastern flank (Figure 4c). This pattern implies that the source of warming might come from the eastern ocean boundary and extend westward along the ASC and then penetrate to the ice shelf front. What is striking in Figure 4c is that the warming in most of the AmIS cavity is higher than 2 °C, even above 2.5 °C in the southern cavity. This is correlated with the very high melting during the

190 last decades of the 21st century in the SSP5-8.5.

The projected temperature changes under SSP1-2.6 scenario (Figure 4d) mirror those under SSP5-8.5. Likewise, a warming of >0.75 °C near the eastern boundary spreads westward, and a much higher warming of >1.5 °C occurs in the AmIS cavity (Figure 4d).

3.2 Mechanism causing the delayed increase in AmIS melting

195 ### 3.2.1 Reversed current induced increase in heat transport

The previous section has shown that the basal melting of AmIS is projected to dramatically increase after 2060 in both scenarios. The following section will explain the reasons for the increased basal melting which is ∼30 years after the onset of warming. According to Liu et al. (2017), PBG and PBECC are the two main import pathways of mCDW into the Amery ice-shelf cavity. Here, we calculate the heat transport (HT) across two zonal transects (indicated by the purple and yellow lines

200 in Figure 5). The meridional HT relative to the surface freezing point (Q) is:
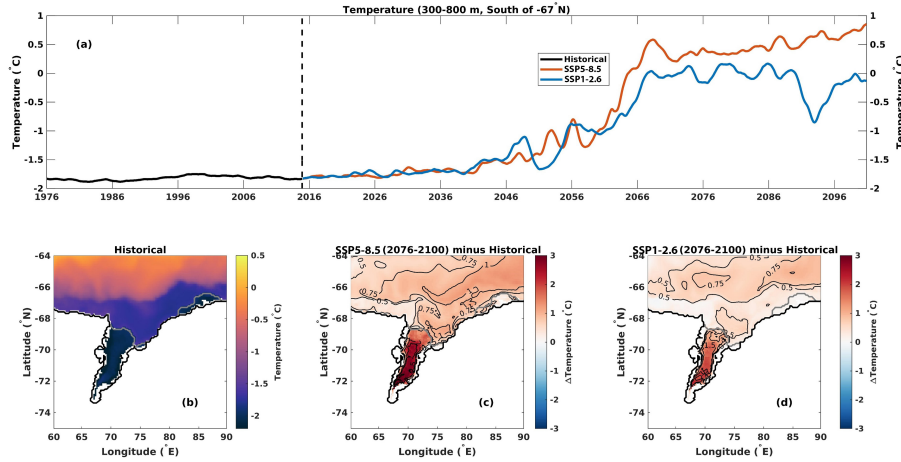
Figure 4. (a) Time series of averaged temperature between 300 and 800 m and on the continental shelf (°C) from 1976 to 2100. A 12-month-running-average is applied. The dashed vertical line indicates the start of 2015. (b) The average of full-depth temperature (°C) over the period of 1976-2014 (Historical). (c) The differences (°C) between the average of full-depth temperature over the period of 2076-2100 under SSP5-8.5 and that of 1976-2014. The warm colours indicate that temperature is projected to increase. The thin black lines represent the temperature differences of 0.5°C, 0.75°C, 1°C, 2°C, 2.5°C. (d) The same as (c) but the SSP1-2.6 experiment. The thin black lines show the temperature differences of 0.5°C, 0.75°C, 1°C, 1.5°C, 2°C. The thick black line represents the coast and the thick grey lines show the ice shelf fronts.

$$Q = \rho C_p \int \int (T - T_f) v \, dz \, dx, \tag{1}$$

where ρ is the seawater density, C_p is the specific heat capacity, T is the seawater temperature, T_f is the surface freezing point temperature and v is the meridional velocity. T and v use the time-mean monthly model outputs.

Figure 6 illustrates the HT of the main flow of PBG, PBECC and TOTAL. The TOTAL is defined as the sum of HT of PBG
205   main flow and PBECC. The HT of PBECC under SSP5-8.5 is always offshore and stable below 0.5×10^{12} J·s^{-1} until 2030 and gradually increases to 2×10^{12} J·s^{-1} by 2100 (Figure 6a). By contrast, the HT of PBG main flow under SSP5-8.5 is stable ($<0.5 \times 10^{12}$ J·s^{-1}) but offshore until 2050 and starts to be unstable before it changes to be permanently onshore in 2064 along with a dramatic jump of $\sim 10 \times 10^{12}$ J·s^{-1} in 2066 under SSP5-8.5. From year 2066 the HT of PBG becomes relatively stable again and eventually experiences a slight increase to $\sim 12 \times 10^{12}$ J·s^{-1} by 2100 (Figure 6a). The TOTAL HT is dominated
210   by PBG main flow. It is generally offshore before 2064 then changes to be constantly onshore, with the increasing amplitude achieving $\sim 12 \times 10^{12}$ J·s^{-1} by 2100 (Figure 6a). This shows that it is the reversal of PBG main flow that brings increased heat into the AmIS cavity from the 2060s, which causes the jump of basal melting and a following stabilisation at a state of high melting.
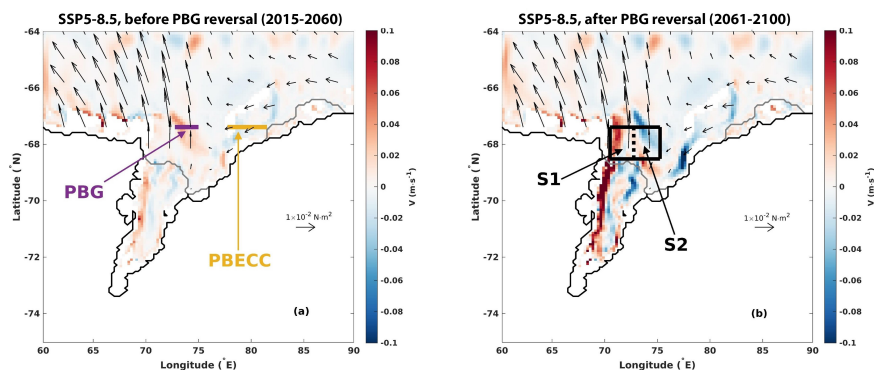
Figure 5. Current pattern (colour) and surface stress (arrows) under SSP5-8.5 scenario (a) before reversal (2015-2060) and (b) after reversal (2061-2100). The colour scale shows the average of meridional velocity (V, $m \cdot s^{-1}$) between 300 and 800 m. The warm colours show the northward current and the cold colours show southward current. The black arrows represent surface stress averaged every eight grids ($10^{-2} N \cdot m^{2}$). The thick purple and yellow lines in (a) indicate the transects of the main flow of PBG and PBECC, respectively. The black boxes in (b) show the locations of local areas S1 and S2 of interest. The northern boundary of S2 is identical to the PBG transect shown in (a).

The HT under SSP1-2.6 shows similar features (Figure 6b). However, there is a notable difference in that the HT of PBG

215   temporarily becomes onshore in about 2090 exclusively under SSP1-2.6 (Figure 6b), which might imply the reversal of PBG main flow is probably not itself irreversible.

The time evolution of HT under SSP5-8.5 and SSP1-2.6 explains the question posed above. Why does the increase of ocean temperature start several decades earlier than that of melt rates? PBG main flow strongly travels northwestward before the 2060s (Figure 5a), it transports most of the heat off-shelf despite the increasing southward HT of PBECC (Figure 6a). This

220   prevents the increasing oceanic heat arriving at the cavity, and consequently delays the increase of melt rates until its reversal.

3.2.2 Freshening driven reversed current

The previous section demonstrated that the reversal of PBG main flow allows the increasing oceanic heat to penetrate the AmIS cavity, causing increased basal melting. We will now discuss what causes the PBG to reverse. The following analysis does not qualitatively vary between SSP5-8.5 and SSP1-2.6, so we only present the results from SSP5-8.5 here.

225   Figure 5 illustrates the depth-averaged meridional velocity between 300-800 m and downward surface stress on the top of ocean before and after the reversal of PBG main flow under SSP5-8.5. It shows that PBG main flow distinctly changes from northward (Figure 5a) to southward (Figure 5b). This is accompanied by a substantially strengthened meltwater outflow coming from beneath the AmIS from the 2060s onward (Figure 5b). However, the changes in surface stress do not agree with the reversal of PBG main flow in our simulations (Figure 5). The surface stress is generally westward over the eastern PB and

230   northwestward over the western PB, exhibiting little change with time (Figure 5). The strong northward component of surface
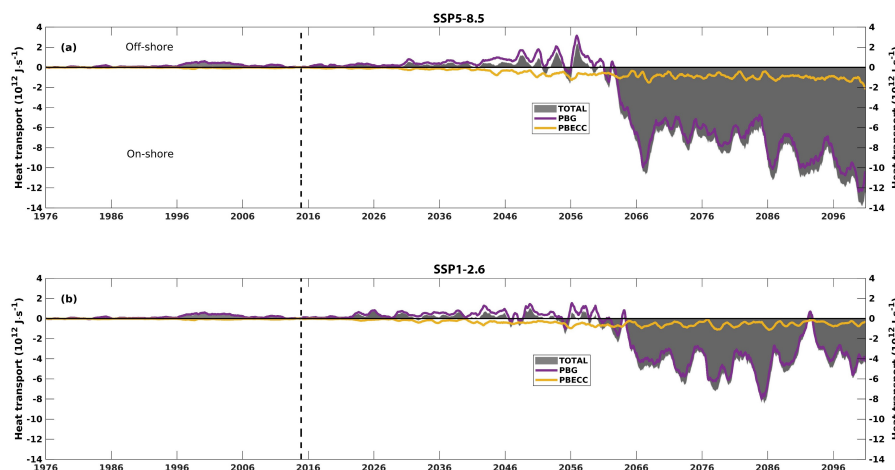
Figure 6. Time series of monthly heat transport (HT, 10^{12} J·s^{-1}) from 1976 to 2100 under (a) SSP5-8.5 scenario and (b) SSP1-2.6 scenario. The purple and yellow lines show the HT of the main flow of Prydz Bay Gyre (PBG) and Prydz Bay Eastern Coastal Current (PBECC), respectively. The grey shaded areas indicate TOTAL HT. TOTAL = PBG + PBECC. The positive/negative values represent the off-shore/on-shore HT. The dashed vertical lines indicate the start of 2015. A 12-month-running-average is applied.

stress over the PBG is contrary to the direction of the PBG since the 2060s (Figure 5b). The wind stress (on the top of ice or ocean when it is sea ice free, not shown) and the surface stress (on the top of ocean) have a similar pattern. This suggests surface stress is not the driver of the flow reversal and that the PBG is more likely to be controlled by density changes.

Here, we focus on the salinity (hence density) changes in two local areas in Amery Depression, S1 and S2 (Figure 5b).
235 Figure 7a shows that the salinity and potential density in S1 which exhibit a drastic decline from surface to bottom between about 2036 and 2060. After 2060, the salinity and density below 300 m recover slightly. However, above 300 m the salinity and density show a further decrease resulting in the steepened density gradients at depth after the late 2060s (Figure 7a). The salinity and density in S2 behave in a similar way (Figure 7b) but with smaller changes. Figure 7c demonstrates the salinity differences between S2 and S1 (hereafter ΔSalinity) and the density differences. There is a substantial redistribution of the
240 salinity and density differences over the period of about 2040 and 2060s when the decrease in salinity is happening. Before 2040, the averaged density in the area S2 is generally ~5×10^{-2} kg·m^{-3} less dense than that in S1. However, the density and salinity in S2 gradually become greater than that in S1 from roughly 2040, and the redistribution spreads from bottom to surface. After 2060 when the differences between the two areas become stable, the density below 300 m in the S2 is generally 10^{-1} kg·m^{-3} denser than that in the S1. Figure 7d illustrates the averaged meridional velocity of PBG main flow along the
245 zonal transect shown in Figure 5. The meridional velocity is stably northward with a maximum velocity of 6-8 cm·s^{-1} below 500 m before 2040. The PBG main flow becomes weakened and unstable, exhibiting high-frequency variability between about 2040-2060. Afterwards, it becomes consistently southward below 200 m and shows the strong velocity of 6-8 $\times10^{-2}$ m·s^{-1} below 500 m.
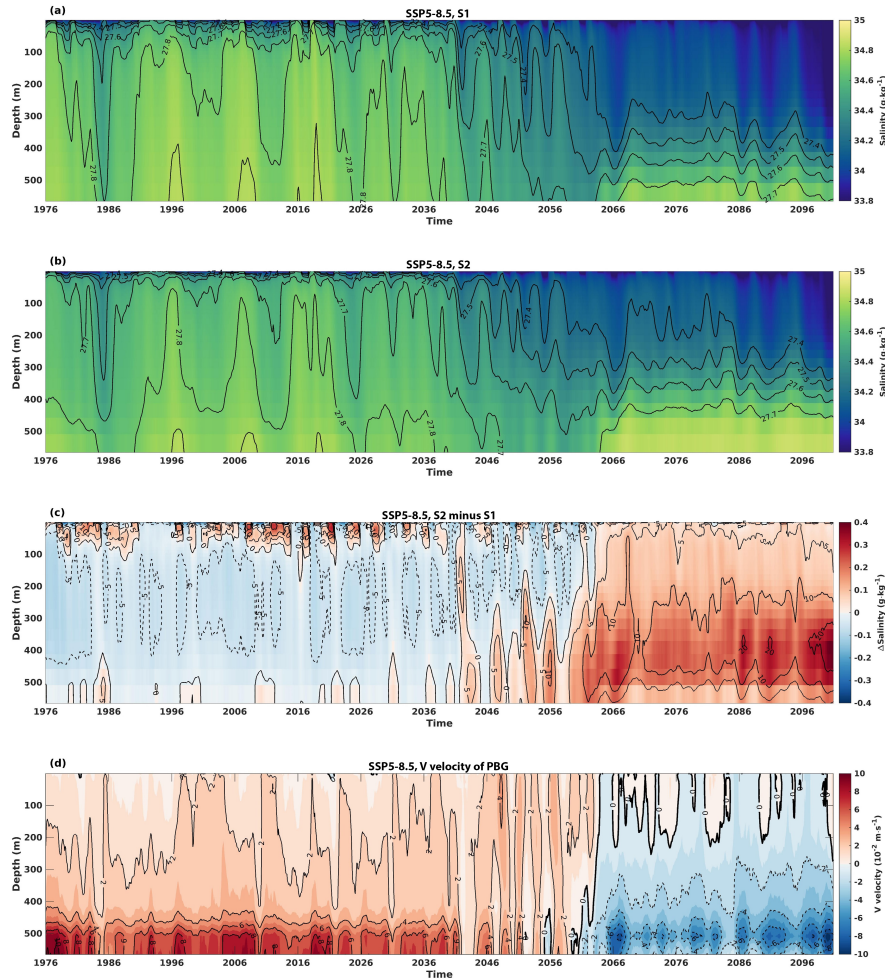
Figure 7. Hovmöller diagram for the spatially averaged salinity (colours, g·kg^{-1}) and potential density (contours, kg·m^{-3}) in (a) S1, (b) S2 in the SSP5-8.5 experiment. The locations of S1 and S2 are shown in Figure 5b. The range of potential density contours is 27.4-27.9 with an interval of 0.1. (c) The differences of salinity (colour, ΔSalinity, g·kg^{-1}) and potential density (contours, 10^{-2} kg·m^{-3}) between S2 and S1. The blue/red colours and the dashed/solid lines represent that S2 is fresher/saltier and lighter/denser than S1. (d) The time-averaged meridional velocity (V, 10^{-2} m·s^{-1}) of the PBG transect shown in Figure 5a. The blue/red colours and the dashed/solid lines indicate southward/northward velocity. The range of velocity contours is -10 to 10 cm·s^{-1} with an interval of 2 cm·s^{-1}. A 12-month-running-average is applied in all time series.

Figure 7 suggests that the current is controlled by the spatial salinity differences between S2 and S1. We suppose that the
250 current is under a geostrophic balance. Here we present a simple estimate of the meridional geostrophic current:

$$fv = \frac{1}{\rho}\frac{dp}{dx}, \tag{2}$$

where f = -1.4×10^{-4} is the Coriolis parameter, v is time-averaged meridional velocity, ρ = 1026 kg·m^{-3} is the seawater density, $dx \approx$ 80 km is distance between S2 and S1 and dp is the pressure difference. Using the hydrostatic hypothesis,

$$dp = gHd\rho, \tag{3}$$

255 where g = 9.81 m·s^{-2} is gravity and $H \approx$ 350 m from Figure 7 is the mean depth. Using a linear equation of state, and assuming that temperature difference do not produce a significant change in density,

$$d\rho = bdS, \tag{4}$$

with b = 0.78 kg·m^3 per thousand, dS is the spatial salinity difference between S2 and S1, and the time-depth-mean dS is approximately equal to -0.1 g·kg^{-1} from 1976-2060 and +0.2 g·kg^{-1} from 2060 onward from Figure 7c. Therefore, the
260 velocity of the time-depth-mean geostrophic current is

$$v = \frac{gHb}{f\rho}\frac{dS}{dx} \approx \begin{cases} +2 \times 10^{-2} \text{ m·s}^{-1}, & \text{before 2060} \\ -5 \times 10^{-2} \text{ m·s}^{-1}, & \text{after 2060} \end{cases} \tag{5}$$

which is within the range of modelled values the magnitude of the modelled velocity shown in Figure 7d.

The analysis above demonstrates that the current is under a geostrophic balance, and the reversal of the flow is a consequence of the reversal of horizontal salinity differences between S2 and S1.

265 Figure 8 further illustrates the freshening-driven reversal. Figure 8a and b show the time-mean of dynamic height anomalies with respect to a reference of 0 dbar before and after the reversal. The dynamic height anomaly is defined as the pressure-integrated specific volume anomaly (IOC et al., 2010). It represents the geostrophic streamfunction for the difference between the pressure level of interest and sea surface (IOC et al., 2010). The dynamic height anomaly was calculated offline with Gibbs-SeaWater (GSW) Oceanographic Toolbox (McDougall and Barker, 2011). We show dynamic height anomalies at 500
270 m because the core of the reversed current is at about 500 m (Figure 7d).

Before the current reversal, the dynamic height anomalies in Amery Depression (AD) vary between -2.5 and -2.1 m^2·s^{-2} with a maximum of about -2.1 m^2·s^{-2} close to the western ice shelf front (Figure 8a). This high centre is accompanied by an anti-clockwise circulation around AD, showing the northward PBG flow (Figure 8a). However, the dynamic height anomalies in AD decrease to -3.5 to -3.2 m^2·s^{-2} during 2061-2100 (Figure 8b). The dynamic height anomalies in the western AD are
275 lowered more than those in the eastern AD. There is a minimum of <-3.5 m^2·s^{-2} near the western ice shelf front that allows currents to flow through the Prydz Bay channel. A new maximum of -3.2 m^2·s^{-2} develops to the eastern bank (Figure 8b). The circulation in AD becomes clockwise following the changes in dynamic height (Figure 8b). Figure 8e shows the time series of the longitude of the dynamic height centre and the time series of AmIS freshwater fluxes. The dynamic height centre is defined as the maximum dynamic height anomalies at 500 m within AD circled by the white line. The changes in the longitude of the

280 dynamic height centre from ∼72°E before 2060 to ∼76°E from 2060 onward (Figure 8c). The evolution of the centre from
the western bank to the eastern bank reflects the reversed horizontal density differences. It coincides with the leap of ice shelf
melting in the 2060s (Figure 8c). This suggests that a stronger freshening happens at 72 °E because it is nearer the outflow of
ISW (Figure 5b), leading to the reversal of horizontal dynamic height in AD. This establishes the new field of dynamic height
anomalies in AD. And the enhanced and continuous ISW outflow sustains the reversed horizontal dynamic height anomalies,
285 hence maintaining the clockwise PBG and the reversed main flow.

The mechanism, in which the freshening at the ice shelf front drives the reversal of PBG main flow, is valid under the SSP1-
2.6 scenario as well (Figure A1). This mechanism is self-maintained: the warm water flushes the sub-ice shelf cavity, and the
strengthened outflow of ice shelf meltwater reverses the salinity differences and stabilises the clockwise gyre, the southward
main flow will carry more warm water to the cavity and sustain the feedback loop. Here comes a remaining question: What
290 triggers the mechanism initially? In other words, what causes the unstable horizontal salinity differences (Figure 7c and A1c)
and the unstable PBG flow (Figure 7d and A1d) between the 2040s and 2060s? On the eastern (upstream) ocean boundary of
our model domain, there is a warming and freshening from 2015 to the 2040s-2050s (Figure A2). This might suggest that the
local warming and freshening near the ice shelf front ultimately come from the upstream ocean boundary. It is also noted that
this mechanism can be interrupted and is reversible. A transient recovery of horizontal salinity difference and the northward
295 PBG main flow in ∼2090 are found in the SSP1-2.6 experiment (Figure A1c, d). This is followed by a decrease in basal melt
rate in ∼2090 (Figure 3a). The reason for this break of the feedback loop is a slight decrease in temperature and an increase in
salinity at the upstream ocean boundary in the 2080s (Figure A2). This emphasises the influences of the upstream systems on
the downstream ice shelves.

4 Conclusions and discussions

300 This study investigates the future changes of AmIS-PB system under SSP5-8.5 and SSP1-2.6 scenarios. An abrupt increase
in AmIS basal melting is projected to happen in the 2060s under both scenarios. The net melt rate of AmIS is projected to
increase from <1 m·yr^{-1} in the 2050s to ∼8 m·yr^{-1} in the late 2060s under SSP1-2.6 and to ∼13 m·yr^{-1} in the late 2060s
under SSP5-8.5. Afterwards, AmIS is in a high melting state until 2100. The time-mean melt rates over 2075-2100 (when it
is in the high melting state) under both SSP1-2.6 and SSP5-8.5 display no refreezing beneath AmIS, and the melting at the
305 grounding line exceeds 30 m·yr^{-1}. A drastic warming on the continental shelf and in the AmIS cavity causes the increased
basal melting. However, the increase of temperature on the continental shelf is in the late 2030s, which happens several decades
before the jump of AmIS basal melting. The delayed increase in AmIS melt rate is due to the reversal of PBG main flow.

PBG plays an important role in heat transport toward AmIS. PBG at the lower depths is not well-established, and the main
flow is northward before ∼the 2060s. This prevents the increased oceanic heat into the AmIS cavity and delays the increase in
310 AmIS melting. However, the main flow of PBG reverses southward after the 2060s as the clockwise PBG is well established.
The southward main flow imports substantial oceanic heat into the cavity, which leads to the increase of AmIS melting. The
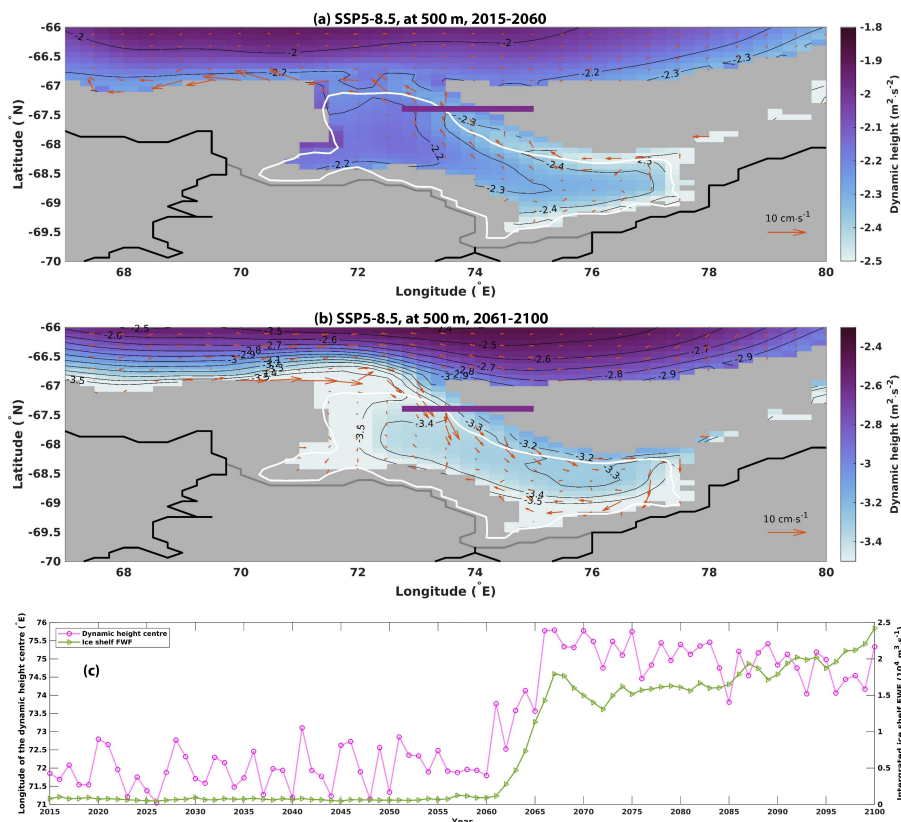
Figure 8. The time-mean of dynamic height anomalies with respect to pressure of 0 dbar (colours and contours, $m^2 \cdot s^{-2}$) is overlaid by the full model current velocity (red arrows, $m \cdot s^{-1}$) under the SSP5-8.5 scenario (a) before (2015-2060), and (b) after (2061-2100) the reversal of PBG main flow. The dynamic height anomalies and the current velocity are at 500 m. Note the different colourmap ranges between (a) and (b). The thick purple lines indicate the main flow of PBG. The white lines are the bathymetry of 530 m, showing the area of Amery Depression (AD) in which the dynamic height centre is defined. The dynamic height centre is chosen as the maximum value in AD. The thick purple lines show the transect of PBG main flow. The black lines indicate the coast. The grey lines represent the ice shelf fronts. (c) Time series of the annual-mean longitude of the dynamic height centre (magenta line) and the ice shelf freshwater flux (FWF, green line).

changes in PBG are due to the reversal of the horizontal salinity (and then density) differences in front of the ice shelf. The redistribution of salinity is established by the strengthened outflow from the AmIS cavity after the 2060s.

This freshening-driven mechanism for PBG is also documented by Galton-Fenzi (2009). In his study, the clockwise PBG does not exist in winter because dense water formed in polynyas blocks the current from the Prydz Bay channel and prevents mCDW from accessing the ice shelf cavity (Galton-Fenzi, 2009). In our simulation, the presence of PBG during the historical period is weak and unstable, showing seasonality in its direction at the upper 200 m (Figure A3b). This seasonality coincides with the strong seasonal reversal of the horizontal differences for salinity and density between S2 and S1 at the upper 200 m (Figure A3a). The weaker horizontal salinity difference at the bottom makes it hard to form the clockwise PBG (Figure A3a).

315

320 However, when the increased ice shelf freshwater freshens the western AD more and reverses the horizontal salinity difference, the clockwise PBG at the lower depths is established after the 2060s (Figure 8). The freshwater forcing to AD helps to form the clockwise PBG, which agrees with Galton-Fenzi (2009). In summary, it is PBG that controls the heat entering the ice shelf cavity, and PBG is determined by the salinity (and density) gradients in AD.

A similar mechanism for re-directed currents is found in front of Filchner-Ronne Ice Shelf (Hellmer et al., 2012, 2017;
325 Naughten et al., 2021; Siahaan et al., 2022) and Ross Ice Shelf (Siahaan et al., 2022). A redirection of inflow is driven by a reversed density gradient across Filchner Trough, which facilitates the penetration of Warm Deep Water into the ice shelf cavity and enhances basal melting. The further freshening due to ice shelf melting maintains the reversal of density gradient and the redirected inflow, leading to further warm penetration and then basal melting (Hellmer et al., 2017). This positive feedback mechanism causes the tipping point of basal mass loss of the Filchner-Ronne Ice Shelf in the 21st century. A re-directed flow
330 in front of Ross Ice Shelf also causes an abrupt increase in basal melting in the second half of the 21st century (Siahaan et al., 2022). The similar processes found in the Filchner-Ronne, Ross and Amery sectors emphasise the importance of buoyancy changes on the shelf sea in a warming future, in particular for a cold ice shelf. Most cold ice shelf sectors have a structure with steep isopycnals at the continental shelf break (Thompson et al., 2018). The geostrophic flow along the isopycnals is sensitive to the structure changes (Thompson et al., 2018). In this study, we only focus on the interactions between AmIS melting and
335 local circulation. However, there remain many open questions for future studies. For example, how does the geostrophic flow respond to different components of freshwater fluxes from ice shelves, sea ice, icebergs, advections, precipitations, etc? What is the role ocean currents play in connecting the future changes in the freshwater components? What is the threshold of freshening on the continental shelf for the re-directed or reversed current? Does the threshold vary among different shelf sea sectors?

Quantifying the future stability of AmIS and its upstream ice sheets is beyond our research scoop, but this study can provide
340 implications to some extent. In our study, AmIS experiences fast basal mass loss during the last decades of the 21st century under the SSP5-8.5 scenario (Figure A4). However, due to the buttressing of the topographic sill at the AmIS grounding line, the fast retreat of the grounding line and large contribution to sea level rise are unlikely to happen (Pittard et al., 2017; Gong et al., 2014). Two previous ice sheet modelling studies (Pittard et al., 2017; Gong et al., 2014) conducted similar extreme experiments by applying enhanced basal melting of AmIS. Both studies suggested that only the collapse of almost the entire
345 ice shelf by unrealistically high basal melting causes the grounding line to retreat beyond the topographic sill. Excluding the most extreme climate scenarios, AmIS attributes to sea level fall (Gong et al., 2014; Pittard et al., 2017). The stability of AmIS and the upstream ice sheets is primarily buttressed by the topographic sill tens of kilometres upstream of the grounding line (Gong et al., 2014; Pittard et al., 2017). It is reasonable to consider that AmIS will remain stable in the next century, however, the fast thinning of the ice shelf (Figure A4) puts AmIS at risk of instability in the longer-term warming future.

350 We note the basal melting in this study might be overestimated. In the AME025 configuration, we use velocity-dependent "three-equation" parameterisation of ice-ocean thermodymanics (Jenkins et al., 2010). This parameterisation assumes that ice shelf melting is driven by the turbulent mixing due to the shear currents. However, the turbulent processes at the ice shelf-ocean interface can also be produced by the convection due to buoyancy forcing (Wells and Worster, 2008). For an ice shelf with a stable stratification at the ice shelf-ocean interface, such as AmIS (Rosevear et al., 2022b), the velocity-dependent "three-

equation" parameterisation largely overestimates basal melting of AmIS by 200%-400% (Rosevear et al., 2022a). This results
in a consequence that the projected melt rate is likely to be overestimated. In addition, UKESM1 has a higher climate sensitivity
compared with other CMIP6 models (Meehl et al., 2020; Forster et al., 2020) and previous generations of climate model (Sellar
et al., 2020). This might produce an overestimated and more rapid warming in our regional projections compared with other
studies (Naughten et al., 2018). Another source of overestimation is the static ice shelf draft. Ice shelf melt rate is not only
temperature dependent (Holland et al., 2008; Xu et al., 2013) but also basal slope dependent (Payne et al., 2007; Little et al.,
2009; Magorrian and Wells, 2016). Steeper slopes might increase the heat entrained into the ice shelf and drive higher melting
(Payne et al., 2007; Little et al., 2009; Magorrian and Wells, 2016). When AmIS is thinning, it will become smoother and
flatter, and the melt rate is expected to be to some extent decreased. Given the limited grounding line retreat of AmIS (Gong
et al., 2014; Pittard et al., 2017), which feeds limited deep and steep grounded ice to the floating AmIS, therefore, the basal
melting beneath the majority of AmIS north of the grounding line may be overestimated. Another limitation is that due to the
relatively coarse grid spacing of ~7-12 km for our model configuration relative to the estimated Rossby radius of 3 km over
Prydz Bay (Liu et al., 2017), we cannot investigate the effect of mesoscale eddies on the AmIS basal melting. Liu et al. (2017)
suggested that 52% of the total onshore heat transport across a zonal transect (73-78°E, 67.5°S) in the Amery ice shelf front
is induced by mesoscale eddies. Given the importance of mesoscale eddy on warm intrusion beneath Antarctic ice shelves
(St-Laurent et al., 2013; Thompson et al., 2018; Stewart et al., 2018, 2019), it is worth employing a higher resolution model
(~1 km) to understand how mesoscale eddies impact future ice shelf melting.

The basal melt rate is projected to exceed 15 m·yr^{-1} beneath the majority of AmIS after the abrupt increase under both
scenarios (Figure 3c, d). The thinning of ice shelf results in many changes, for instance, the geometry of the ice shelf cavity,
the increased water column thickness under the ice shelf, etc. This is related to a scientific question: How does time-varying ice
shelf draft modify ocean circulations in the cavity and ice shelf-ocean interactions in model simulations? Holland et al. (2023)
suggests that a time-varying ice geometry of Thwaites Glacier leads to an increase in melting by more than 30% without any
change in ocean forcing. However, we use a static ice shelf draft in the AME025 configuration, which limits the ability to
investigate such geometrical feedback. Future work would greatly benefit from the development of two-way coupled ocean-ice
sheet models and more sophisticated Earth system models (Jordan et al., 2018; Smith et al., 2021; Siahaan et al., 2022; De Rydt
and Naughten, 2023).
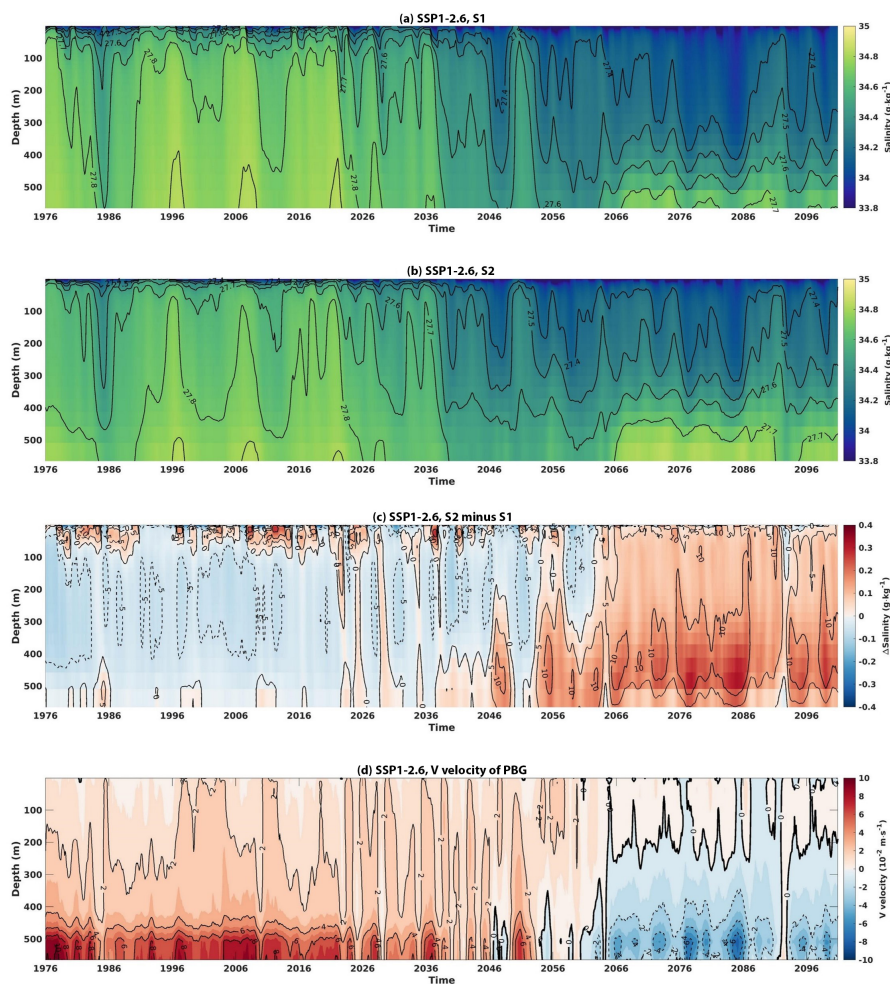
Figure A1. Hovmöller diagram for the spatially averaged salinity (colour, g·kg^{-1}) and potential density (contours, kg·m^{-3}) in (a) S1, (b) S2 in the SSP1-2.6 experiment. The locations of S1 and S2 are shown in Figure 5b. The range of potential density contours is 27.4-27.9 with an interval of 0.1. (c) The differences of salinity (colour, ΔSalinity, g·kg^{-1}) and potential density (contours, 10^{-2} kg·m^{-3}) between S2 and S1. The blue/red colours and the dashed/solid lines represent that S2 is fresher/saltier and lighter/denser than S1. (d) The time-averaged meridional velocity (V, cm·s^{-1}) of the PBG transect shown in Figure 5a. The blue/red colours and the dashed/solid lines indicate southward/northward velocity. The range of velocity contours is -10 to 10 cm·s^{-1} with an interval of 2 cm·s^{-1}. A 12-month-running-average is applied in all time series.

Figure A2. (a) Time series of averaged temperature of ocean boundary forcing at the upstream boundary from 1976 to 2100. A 12-month-running-average is applied. The dashed vertical line indicates the start of 2015. (b) The same but for salinity ocean boundary forcing.
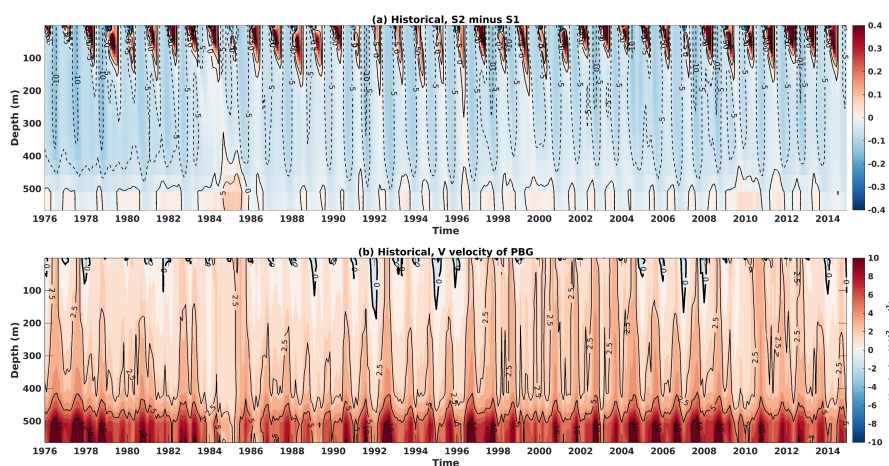
Figure A3. (a) Hovmöller diagram for the monthly spatially-averaged differences of salinity (colours, ΔSalinity, g·kg^{-1}) and potential density (contours, 10^{-2} kg·m^{-3}) between S2 and S1. The blue/red colours and the dashed/solid lines represent that S2 is fresher/saltier and lighter/denser than S1. (d) The time-averaged meridional velocity (V, cm·s^{-1}) of the PBG transect shown in Figure 5a. The blue/red colours and the dashed/solid lines indicate southward/northward velocity.

Appendix A: Extra figures

A1 Extra figures for the SSP1-2.6 experiment

A2 The forcing of temperature and salinity at the upstream ocean boundary

A3 Monthly salinity difference between S2 and S1 and the meridional velocity of the PBG during the historical period

A4 Basal mass loss of AmIS

385
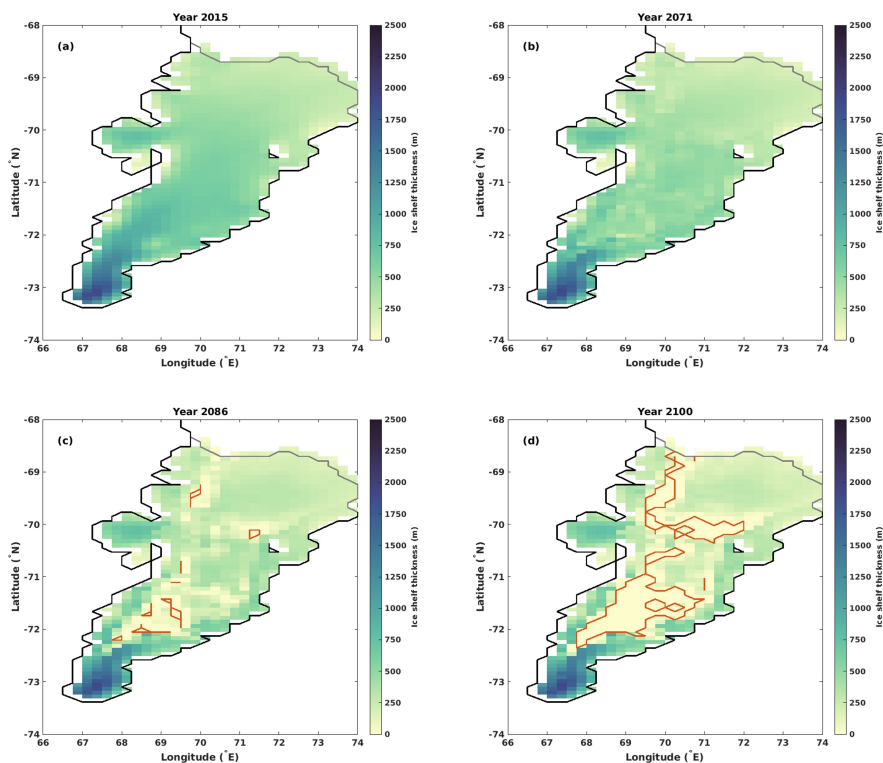
Figure A4. Basal mass loss of AmIS. Snapshot of AmIS ice shelf thickness (m) in year (a) 2015, (b) 2071, (c) 2086, (d) 2100 under SSP5-8.5 scenario. The red lines represent ice shelf thickness of 0 m, indicating that the ice is removed by basal melting.

Author contributions. JJ conducted the ocean simulations and prepared the manuscript. AP and CB helped to set up the regional model configuration and helped to interpret analysis. All authors commented on the manuscript.

Competing interests. The authors declare that they have no conflict of interest.

Acknowledgements. Jing Jin and Antony Payne were supported by OCEAN:ICE, which is co-funded by the European Union, Horizon Europe Funding Programme for research and innovation under grant agreement Nr. 101060452 and by UK Research and Innovation. O:I Contribution number 9. Christopher Bull was supported by the European Union's Horizon 2020 research and innovation programme under grant agreement no. 820575 (TiPACCs). The modelling work was carried out using the computational facilities of the Advanced Computing Research Centre, University of Bristol - http://www.bristol.ac.uk/acrc/.

References

Adusumilli, S., Fricker, H. A., Medley, B., Padman, L., and Siegfried, M. R.: Interannual variations in meltwater input to the Southern Ocean
from Antarctic ice shelves, NATURE GEOSCIENCE, 13, 616+, https://doi.org/10.1038/s41561-020-0616-z, 2020.

Allison, I.: The Mass Budget of the Lambert Glacier Drainage Basin, Antarctica, Journal of Glaciology, 22, 223–235,
https://doi.org/10.3189/S0022143000014222, 1979.

Amante, C. and Eakins, B. W.: ETOPO1 arc-minute global relief model : procedures, data sources and analysis, https://repository.library.
noaa.gov/view/noaa/1163, technical Memorandum, 2009.

Aoki, S., Takahashi, T., Yamazaki, K., Hirano, D., Ono, K., Kusahara, K., Tamura, T., and Williams, G. D.: Warm surface waters increase
Antarctic ice shelf melt and delay dense water formation, Communications Earth & Environment, 3, 142, https://doi.org/10.1038/s43247-
022-00456-z, 2022.

Arakawa, A. and Lamb, V. R.: A Potential Enstrophy and Energy Conserving Scheme for the Shallow Water Equations, Monthly Weather
Review, 109, 18 – 36, https://doi.org/10.1175/1520-0493(1981)109<0018:APEAEC>2.0.CO;2, 1981.

Arndt, J. E., Schenke, H. W., Jakobsson, M., Nitsche, F. O., Buys, G., Goleby, B., Rebesco, M., Bohoyo, F., Hong, J., Black, J., Greku, R.,
Udintsev, G., Barrios, F., Reynoso-Peralta, W., Taisei, M., and Wigley, R.: The International Bathymetric Chart of the Southern Ocean
(IBCSO) Version 1.0—A new bathymetric compilation covering circum-Antarctic waters, Geophysical Research Letters, 40, 3111–3117,
https://doi.org/https://doi.org/10.1002/grl.50413, 2013.

Beadling, R. L., Russell, J. L., Stouffer, R. J., Mazloff, M., Talley, L. D., Goodman, P. J., Sallée, J. B., Hewitt, H. T., Hyder, P., and Pandde,
A.: Representation of Southern Ocean Properties across Coupled Model Intercomparison Project Generations: CMIP3 to CMIP6, Journal
of Climate, 33, 6555 – 6581, https://doi.org/10.1175/JCLI-D-19-0970.1, 2020.

Bracegirdle, T. J., Holmes, C. R., Hosking, J. S., Marshall, G. J., Osman, M., Patterson, M., and Rackow, T.: Improvements in Cir-
cumpolar Southern Hemisphere Extratropical Atmospheric Circulation in CMIP6 Compared to CMIP5, Earth and Space Science, 7,
e2019EA001 065, https://doi.org/https://doi.org/10.1029/2019EA001065, 2020.

Bull, C. Y. S., Jenkins, A., Jourdain, N. C., Vaňková, I., Holland, P. R., Mathiot, P., Hausmann, U., and Sallée, J.-B.: Remote Control of
Filchner-Ronne Ice Shelf Melt Rates by the Antarctic Slope Current, Journal of Geophysical Research: Oceans, 126, e2020JC016 550,
https://doi.org/https://doi.org/10.1029/2020JC016550, e2020JC016550 2020JC016550, 2021.

Chen, H., Rignot, E., Scheuchl, B., and Ehrenfeucht, S.: Grounding Zone of Amery Ice Shelf, Antarctica,
From Differential Synthetic-Aperture Radar Interferometry, Geophysical Research Letters, 50, e2022GL102 430,
https://doi.org/https://doi.org/10.1029/2022GL102430, e2022GL102430 2022GL102430, 2023.

Craven, M., Allison, I., Brand, R., Elcheikh, A., Hunter, J., Hemer, M., and Donoghue, S.: Initial borehole results from the Amery Ice Shelf
hot-water drilling project, Annals of Glaciology, 39, 531–539, https://doi.org/10.3189/172756404781814311, 2004.

Craven, M., Allison, I., Fricker, H. A., and Warner, R.: Properties of a marine ice layer under the Amery Ice Shelf, East Antarctica, Journal
of Glaciology, 55, 717–728, https://doi.org/10.3189/002214309789470941, 2009.

De Rydt, J. and Naughten, K.: Geometric amplification and suppression of ice-shelf basal melt in West Antarctica, EGUsphere [preprint],
2023, 1–36, https://doi.org/10.5194/egusphere-2023-1587, 2023.

Depoorter, M. A., Bamber, J. L., Griggs, J. A., Lenaerts, J. T. M., Ligtenberg, S. R. M., van den Broeke, M. R., and Moholdt, G.: Calving
fluxes and basal melt rates of Antarctic ice shelves, NATURE, 502, 89+, https://doi.org/10.1038/nature12567, 2013.

Forster, P. M., Maycock, A. C., McKenna, C. M., and Smith, C. J.: Latest climate models confirm need for urgent mitigation, Nature Climate Change, 10, 7–10, https://doi.org/10.1038/s41558-019-0660-0, 2020.

Fox-Kemper, B., Hewitt, H., Xiao, C., Aðalgeirsdóttir, G., Drijfhout, S., Edwards, T., Golledge, N., Hemer, M., Kopp, R., Krinner, G., Mix, A., Notz, D., Nowicki, S., Nurhati, I., Ruiz, L., Sallée, J.-B., Slangen, A., and Yu, Y.: Ocean, Cryosphere and Sea Level Change, p. 1211–1362, Cambridge University Press, Cambridge, United Kingdom and New York, NY, USA, https://doi.org/10.1017/9781009157896.011, 2021.

Fretwell, P., Pritchard, H. D., Vaughan, D. G., Bamber, J. L., Barrand, N. E., Bell, R., Bianchi, C., Bingham, R. G., Blankenship, D. D., Casassa, G., Catania, G., Callens, D., Conway, H., Cook, A. J., Corr, H. F. J., Damaske, D., Damm, V., Ferraccioli, F., Forsberg, R., Fujita, S., Gim, Y., Gogineni, P., Griggs, J. A., Hindmarsh, R. C. A., Holmlund, P., Holt, J. W., Jacobel, R. W., Jenkins, A., Jokat, W., Jordan, T., King, E. C., Kohler, J., Krabill, W., Riger-Kusk, M., Langley, K. A., Leitchenkov, G., Leuschen, C., Luyendyk, B. P., Matsuoka, K., Mouginot, J., Nitsche, F. O., Nogi, Y., Nost, O. A., Popov, S. V., Rignot, E., Rippin, D. M., Rivera, A., Roberts, J., Ross, N., Siegert, M. J., Smith, A. M., Steinhage, D., Studinger, M., Sun, B., Tinto, B. K., Welch, B. C., Wilson, D., Young, D. A., Xiangbin, C., and Zirizzotti, A.: Bedmap2: improved ice bed, surface and thickness datasets for Antarctica, The Cryosphere, 7, 375–393, https://doi.org/10.5194/tc-7-375-2013, 2013.

Galton-Fenzi, B. K.: Modelling ice-shelf/ocean interaction, Ph.D. thesis, University of Tasmania, Hobart, Australia, 2009.

Galton-Fenzi, B. K., Maraldi, C., Coleman, R., and Hunter, J.: The cavity under the Amery Ice Shelf, East Antarctica, Journal of Glaciology, 54, 881–887, https://doi.org/10.3189/002214308787779898, 2008.

Galton-Fenzi, B. K., Hunter, J. R., Coleman, R., Marsland, S. J., and Warner, R. C.: Modeling the basal melting and marine ice accretion of the Amery Ice Shelf, Journal of Geophysical Research: Oceans, 117, https://doi.org/https://doi.org/10.1029/2012JC008214, 2012.

Gong, Y., Cornford, S. L., and Payne, A. J.: Modelling the response of the Lambert Glacier–Amery Ice Shelf system, East Antarctica, to uncertain climate forcing over the 21st and 22nd centuries, The Cryosphere, 8, 1057–1068, https://doi.org/10.5194/tc-8-1057-2014, 2014.

Good, P., Sellar, A., Tang, Y., Rumbold, S., Ellis, R., Kelley, D., and Kuhlbrodt, T.: MOHC UKESM1.0-LL model output prepared for CMIP6 ScenarioMIP ssp126, https://doi.org/10.22033/ESGF/CMIP6.6333, 2019a.

Good, P., Sellar, A., Tang, Y., Rumbold, S., Ellis, R., Kelley, D., and Kuhlbrodt, T.: MOHC UKESM1.0-LL model output prepared for CMIP6 ScenarioMIP ssp585, https://doi.org/10.22033/ESGF/CMIP6.6405, 2019b.

Guo, G., Shi, J., Gao, L., Tamura, T., and Williams, G. D.: Reduced Sea Ice Production Due to Upwelled Oceanic Heat Flux in Prydz Bay, East Antarctica, Geophysical Research Letters, 46, 4782–4789, https://doi.org/https://doi.org/10.1029/2018GL081463, 2019.

Guo, G., Gao, L., Shi, J., and Zu, Y.: Wind-Driven Seasonal Intrusion of Modified Circumpolar Deep Water Onto the Continental Shelf in Prydz Bay, East Antarctica, Journal of Geophysical Research: Oceans, 127, e2022JC018 741, https://doi.org/https://doi.org/10.1029/2022JC018741, e2022JC018741 2022JC018741, 2022.

Gurvan, M., Bourdallé-Badie, R., Bouttier, P.-A., Bricaud, C., Bruciaferri, D., Calvert, D., Chanut, J., Clementi, E., Coward, A., Delrosso, D., Ethé, C., Flavoni, S., Graham, T., Harle, J., Iovino, D., Lea, D., Lévy, C., Lovato, T., Martin, N., Masson, S., Mocavero, S., Paul, J., Rousset, C., Storkey, D., Storto, A., and Vancoppenolle, M.: NEMO ocean engine, https://doi.org/10.5281/zenodo.3248739, Fix broken cross-references, still revision 8625 from SVN repository., 2017.

Hellmer, H. H., Kauker, F., Timmermann, R., Determann, J., and Rae, J.: Twenty-first-century warming of a large Antarctic ice-shelf cavity by a redirected coastal current, NATURE, 485, 225–228, https://doi.org/10.1038/nature11064, 2012.

Hellmer, H. H., Kauker, F., Timmermann, R., and Hattermann, T.: The Fate of the Southern Weddell Sea Continental Shelf in a Warming Climate, Journal of Climate, 30, 4337 – 4350, https://doi.org/10.1175/JCLI-D-16-0420.1, 2017.

Herraiz-Borreguero, L., Coleman, R., Allison, I., Rintoul, S. R., Craven, M., and Williams, G. D.: Circulation of modified Circumpolar Deep Water and basal melt beneath the Amery Ice Shelf, East Antarctica, Journal of Geophysical Research: Oceans, 120, 3098–3112, https://doi.org/https://doi.org/10.1002/2015JC010697, 2015.

475 Herraiz-Borreguero, L., Church, J. A., Allison, I., Peña-Molino, B., Coleman, R., Tomczak, M., and Craven, M.: Basal melt, seasonal water mass transformation, ocean current variability, and deep convection processes along the Amery Ice Shelf calving front, East Antarctica, Journal of Geophysical Research: Oceans, 121, 4946–4965, https://doi.org/https://doi.org/10.1002/2016JC011858, 2016.

Heuzé, C.: Antarctic Bottom Water and North Atlantic Deep Water in CMIP6 models, Ocean Science, 17, 59–90, https://doi.org/10.5194/os-17-59-2021, 2021.

480 Heywood, K. J., Sparrow, M. D., Brown, J., and Dickson, R. R.: Frontal structure and Antarctic Bottom Water flow through the Princess Elizabeth Trough, Antarctica, Deep Sea Research Part I: Oceanographic Research Papers, 46, 1181–1200, https://doi.org/https://doi.org/10.1016/S0967-0637(98)00108-3, 1999.

Holland, P. R., Jenkins, A., and Holland, D. M.: The Response of Ice Shelf Basal Melting to Variations in Ocean Temperature, Journal of Climate, 21, 2558 – 2572, https://doi.org/https://doi.org/10.1175/2007JCLI1909.1, 2008.

485 Holland, P. R., Bevan, S. L., and Luckman, A. J.: Strong Ocean Melting Feedback During the Recent Retreat of Thwaites Glacier, Geophysical Research Letters, 50, e2023GL103 088, https://doi.org/https://doi.org/10.1029/2023GL103088, 2023.

IOC, IHO, and BODC.: GEBCO Digital Atlas : Centenary edition of the IHO/IOC General Bathymetric Chart of the Oceans., British Oceanographic Data Centre, Liverpool, 2003.

IOC, SCOR, and IAPSO: The international thermodynamic equation of seawater–2010: Calculation and use of thermodynamic properties,
490 Intergovernmental Oceanographic Commission, Manuals and Guides No. 56, 56, 196, https://www.teos-10.org/, 2010.

Jenkins, A., Nicholls, K. W., and Corr, H. F. J.: Observation and Parameterization of Ablation at the Base of Ronne Ice Shelf, Antarctica, Journal of Physical Oceanography, 40, 2298 – 2312, https://doi.org/10.1175/2010JPO4317.1, 2010.

Jordan, J. R., Holland, P. R., Goldberg, D., Snow, K., Arthern, R., Campin, J.-M., Heimbach, P., and Jenkins, A.: Ocean-Forced Ice-Shelf Thinning in a Synchronously Coupled Ice-Ocean Model, Journal of Geophysical Research: Oceans, 123, 864–882,
495 https://doi.org/https://doi.org/10.1002/2017JC013251, 2018.

Jourdain, N. C., Mathiot, P., Merino, N., Durand, G., Le Sommer, J., Spence, P., Dutrieux, P., and Madec, G.: Ocean circulation and sea-ice thinning induced by melting ice shelves in the Amundsen Sea, Journal of Geophysical Research: Oceans, 122, 2550–2573, https://doi.org/https://doi.org/10.1002/2016JC012509, 2017.

Kusahara, K., Tatebe, H., Hajima, T., Saito, F., and Kawamiya, M.: Antarctic Sea Ice Holds the Fate of Antarctic Ice-Shelf Basal Melting in
500 a Warming Climate, Journal of Climate, 36, 713 – 743, https://doi.org/https://doi.org/10.1175/JCLI-D-22-0079.1, 2023.

Large, W. and Yeager, S.: Diurnal to Decadal Global Forcing for Ocean and Sea-Ice Models: The Data Sets and Flux Climatologies (No. NCAR/TN-460+STR), Tech. rep., https://doi.org/10.5065/D6KK98Q6, 2004.

Little, C. M., Gnanadesikan, A., and Oppenheimer, M.: How ice shelf morphology controls basal melting, Journal of Geophysical Research: Oceans, 114, https://doi.org/https://doi.org/10.1029/2008JC005197, 2009.

505 Liu, C., Wang, Z., Cheng, C., Xia, R., Li, B., and Xie, Z.: Modeling modified Circumpolar Deep Water intrusions onto the Prydz Bay continental shelf, East Antarctica, Journal of Geophysical Research: Oceans, 122, 5198–5217, https://doi.org/https://doi.org/10.1002/2016JC012336, 2017.

Liu, C., Wang, Z., Cheng, C., Wu, Y., Xia, R., Li, B., and Li, X.: On the Modified Circumpolar Deep Water Upwelling Over the Four Ladies Bank in Prydz Bay, East Antarctica, Journal of Geophysical Research: Oceans, 123, 7819–7838, https://doi.org/https://doi.org/10.1029/2018JC014026, 2018.

510

Magorrian, S. J. and Wells, A. J.: Turbulent plumes from a glacier terminus melting in a stratified ocean, Journal of Geophysical Research: Oceans, 121, 4670–4696, https://doi.org/https://doi.org/10.1002/2015JC011160, 2016.

Marsh, R., Ivchenko, V. O., Skliris, N., Alderson, S., Bigg, G. R., Madec, G., Blaker, A. T., Aksenov, Y., Sinha, B., Coward, A. C., Le Sommer, J., Merino, N., and Zalesny, V. B.: NEMO–ICB (v1.0): interactive icebergs in the NEMO ocean model globally configured at eddy-permitting resolution, Geoscientific Model Development, 8, 1547–1562, https://doi.org/10.5194/gmd-8-1547-2015, 2015.

515

Mathiot, P. and Jourdain, N. C.: Southern Ocean warming and Antarctic ice shelf melting in conditions plausible by late 23rd century in a high-end scenario, Ocean Science, 19, 1595–1615, https://doi.org/10.5194/os-19-1595-2023, 2023.

Mathiot, P., Goosse, H., Fichefet, T., Barnier, B., and Gallée, H.: Modelling the seasonal variability of the Antarctic Slope Current, Ocean Science, 7, 455–470, https://doi.org/10.5194/os-7-455-2011, 2011.

520

Mathiot, P., Jenkins, A., Harris, C., and Madec, G.: Explicit representation and parametrised impacts of under ice shelf seas in the z^* coordinate ocean model NEMO 3.6, Geoscientific Model Development, 10, 2849–2874, https://doi.org/10.5194/gmd-10-2849-2017, 2017.

McDougall, T. J. and Barker, P. M.: Getting started with TEOS-10 and the Gibbs Seawater (GSW) Oceanographic Toolbox, Tech. rep., SCOR/IAPSO WG127, 2011.

Meehl, G. A., Senior, C. A., Eyring, V., Flato, G., Lamarque, J.-F., Stouffer, R. J., Taylor, K. E., and Schlund, M.: Context for interpreting equilibrium climate sensitivity and transient climate response from the CMIP6 Earth system models, Science Advances, 6, eaba1981, https://doi.org/10.1126/sciadv.aba1981, 2020.

525

Naughten, K. A., Meissner, K. J., Galton-Fenzi, B. K., England, M. H., Timmermann, R., and Hellmer, H. H.: Future Projections of Antarctic Ice Shelf Melting Based on CMIP5 Scenarios, Journal of Climate, 31, 5243 – 5261, https://doi.org/10.1175/JCLI-D-17-0854.1, 2018.

Naughten, K. A., De Rydt, J., Rosier, S. H. R., Jenkins, A., Holland, P. R., and Ridley, J. K.: Two-timescale response of a large Antarctic ice shelf to climate change, NATURE COMMUNICATIONS, 12, https://doi.org/10.1038/s41467-021-22259-0, 2021.

530

Nunes Vaz, R. A. and Lennon, G. W.: Physical oceanography of the Prydz Bay region of Antarctic waters, Deep Sea Research Part I: Oceanographic Research Papers, 43, 603–641, https://doi.org/https://doi.org/10.1016/0967-0637(96)00028-3, 1996.

O'Brien, P. E., Harris, P. T., Post, A. L., and Young, N.: Chapter 18 East Antarctic continental shelf: Prydz Bay and the Mac.Robertson Land Shelf, Geological Society, London, Memoirs, 41, 241–254, https://doi.org/10.1144/M41.18, 2014.

535

Ohshima, K. I., Fukamachi, Y., Williams, G. D., Nihashi, S., Roquet, F., Kitade, Y., Tamura, T., Hirano, D., Herraiz-Borreguero, L., Field, I., Hindell, M., Aoki, S., and Wakatsuchi, M.: Antarctic BottomWater production by intense sea-ice formation in the Cape Darnley polynya, NATURE GEOSCIENCE, 6, 235–240, https://doi.org/10.1038/NGEO1738, 2013.

Payne, A. J., Holland, P. R., Shepherd, A. P., Rutt, I. C., Jenkins, A., and Joughin, I.: Numerical modeling of ocean-ice interactions under Pine Island Bay's ice shelf, Journal of Geophysical Research: Oceans, 112, https://doi.org/https://doi.org/10.1029/2006JC003733, 2007.

540

Pittard, M. L., Galton-Fenzi, B. K., Watson, C. S., and Roberts, J. L.: Future sea level change from Antarctica's Lambert-Amery glacial system, Geophysical Research Letters, 44, 7347–7355, https://doi.org/https://doi.org/10.1002/2017GL073486, 2017.

Portela, E., Rintoul, S. R., Bestley, S., Herraiz-Borreguero, L., van Wijk, E., McMahon, C. R., Roquet, F., and Hindell, M.: Seasonal Transformation and Spatial Variability of Water Masses Within MacKenzie Polynya, Prydz Bay, Journal of Geophysical Research: Oceans, 126, e2021JC017 748, https://doi.org/https://doi.org/10.1029/2021JC017748, 2021.

545 Purich, A. and England, M. H.: Historical and Future Projected Warming of Antarctic Shelf Bottom Water in CMIP6 Models, Geophysical Research Letters, 48, e2021GL092 752, https://doi.org/https://doi.org/10.1029/2021GL092752, 2021.

Rignot, E., Jacobs, S., Mouginot, J., and Scheuchl, B.: Ice-Shelf Melting Around Antarctica, SCIENCE, 341, 266–270, https://doi.org/10.1126/science.1235798, 2013.

Rintoul, S. R., Chown, S. L., DeConto, R. M., England, M. H., Fricker, H. A., Masson-Delmotte, V., Naish, T. R., Siegert, M. J., and Xavier,
550 J. C.: Choosing the future of Antarctica, Nature, 558, 233–241, https://doi.org/10.1038/s41586-018-0173-4, 2018.

Roach, L. A., Dörr, J., Holmes, C. R., Massonnet, F., Blockley, E. W., Notz, D., Rackow, T., Raphael, M. N., O'Farrell, S. P., Bailey, D. A., and Bitz, C. M.: Antarctic Sea Ice Area in CMIP6, Geophysical Research Letters, 47, e2019GL086 729, https://doi.org/https://doi.org/10.1029/2019GL086729, 2020.

Roquet, F., Madec, G., McDougall, T. J., and Barker, P. M.: Accurate polynomial expressions for the density and specific volume of seawater
555 using the TEOS-10 standard, Ocean Modelling, 90, 29–43, https://doi.org/https://doi.org/10.1016/j.ocemod.2015.04.002, 2015.

Rosevear, M., Galton-Fenzi, B., and Stevens, C.: Evaluation of basal melting parameterisations using in situ ocean and melting observations from the Amery Ice Shelf, East Antarctica, Ocean Science, 18, 1109–1130, https://doi.org/10.5194/os-18-1109-2022, 2022a.

Rosevear, M. G., Gayen, B., and Galton-Fenzi, B. K.: Regimes and Transitions in the Basal Melting of Antarctic Ice Shelves, Journal of Physical Oceanography, 52, 2589 – 2608, https://doi.org/10.1175/JPO-D-21-0317.1, 2022b.

560 Rousset, C., Vancoppenolle, M., Madec, G., Fichefet, T., Flavoni, S., Barthélemy, A., Benshila, R., Chanut, J., Levy, C., Masson, S., and Vivier, F.: The Louvain-La-Neuve sea ice model LIM3.6: global and regional capabilities, Geoscientific Model Development, 8, 2991–3005, https://doi.org/10.5194/gmd-8-2991-2015, 2015.

Sellar, A. A., Walton, J., Jones, C. G., Wood, R., Abraham, N. L., Andrejczuk, M., Andrews, M. B., Andrews, T., Archibald, A. T., de Mora, L., Dyson, H., Elkington, M., Ellis, R., Florek, P., Good, P., Gohar, L., Haddad, S., Hardiman, S. C., Hogan, E., Iwi, A., Jones, C. D.,
565 Johnson, B., Kelley, D. I., Kettleborough, J., Knight, J. R., Köhler, M. O., Kuhlbrodt, T., Liddicoat, S., Linova-Pavlova, I., Mizielinski, M. S., Morgenstern, O., Mulcahy, J., Neininger, E., O'Connor, F. M., Petrie, R., Ridley, J., Rioual, J.-C., Roberts, M., Robertson, E., Rumbold, S., Seddon, J., Shepherd, H., Shim, S., Stephens, A., Teixiera, J. C., Tang, Y., Williams, J., Wiltshire, A., and Griffiths, P. T.: Implementation of U.K. Earth System Models for CMIP6, Journal of Advances in Modeling Earth Systems, 12, e2019MS001 946, https://doi.org/https://doi.org/10.1029/2019MS001946, 2020.

570 Siahaan, A., Smith, R. S., Holland, P. R., Jenkins, A., Gregory, J. M., Lee, V., Mathiot, P., Payne, A. J., Ridley, J. K., and Jones, C. G.: The Antarctic contribution to 21st-century sea-level rise predicted by the UK Earth System Model with an interactive ice sheet, The Cryosphere, 16, 4053–4086, https://doi.org/10.5194/tc-16-4053-2022, 2022.

Smith, N. R., Zhaoqian, D., Kerry, K. R., and Wright, S.: Water masses and circulation in the region of Prydz Bay, Antarctica, Deep Sea Research Part A. Oceanographic Research Papers, 31, 1121–1147, https://doi.org/https://doi.org/10.1016/0198-0149(84)90016-5, 1984.

575 Smith, R. S., Mathiot, P., Siahaan, A., Lee, V., Cornford, S. L., Gregory, J. M., Payne, A. J., Jenkins, A., Holland, P. R., Ridley, J. K., and Jones, C. G.: Coupling the U.K. Earth System Model to Dynamic Models of the Greenland and Antarctic Ice Sheets, Journal of Advances in Modeling Earth Systems, 13, e2021MS002 520, https://doi.org/https://doi.org/10.1029/2021MS002520, 2021.

Spence, P., Holmes, R. M., Hogg, A. M., Griffies, S. M., Stewart, K. D., and England, M. H.: Localized rapid warming of West Antarctic subsurface waters by remote winds, NATURE CLIMATE CHANGE, 7, 595–603, https://doi.org/10.1038/NCLIMATE3335, 2017.

580 St-Laurent, P., Klinck, J. M., and Dinniman, M. S.: On the Role of Coastal Troughs in the Circulation of Warm Circumpolar Deep Water on Antarctic Shelves, Journal of Physical Oceanography, 43, 51 – 64, https://doi.org/10.1175/JPO-D-11-0237.1, 2013.

Stewart, A. L., Klocker, A., and Menemenlis, D.: Circum-Antarctic Shoreward Heat Transport Derived From an Eddy- and Tide-Resolving Simulation, Geophysical Research Letters, 45, 834–845, https://doi.org/https://doi.org/10.1002/2017GL075677, 2018.

585 Stewart, A. L., Klocker, A., and Menemenlis, D.: Acceleration and Overturning of the Antarctic Slope Current by Winds, Eddies, and Tides, Journal of Physical Oceanography, 49, 2043 – 2074, https://doi.org/10.1175/JPO-D-18-0221.1, 2019.

Storkey, D., Blaker, A. T., Mathiot, P., Megann, A., Aksenov, Y., Blockley, E. W., Calvert, D., Graham, T., Hewitt, H. T., Hyder, P., Kuhlbrodt, T., Rae, J. G. L., and Sinha, B.: UK Global Ocean GO6 and GO7: a traceable hierarchy of model resolutions, Geoscientific Model Development, 11, 3187–3213, https://doi.org/10.5194/gmd-11-3187-2018, 2018.

Tang, Y., Rumbold, S., Ellis, R., Kelley, D., Mulcahy, J., Sellar, A., Walton, J., and Jones, C.: MOHC UKESM1.0-LL model output prepared

590 for CMIP6 CMIP historical, https://doi.org/10.22033/ESGF/CMIP6.6113, 2019.

Thomas, M., Ridley, J. K., Smith, I. J., Stevens, D. P., Holland, P. R., and Mackie, S.: Future Response of Antarctic Continental Shelf Temperatures to Ice Shelf Basal Melting and Calving, Geophysical Research Letters, 50, e2022GL102 101, https://doi.org/https://doi.org/10.1029/2022GL102101, e2022GL102101 2022GL102101, 2023.

Thompson, A. F., Stewart, A. L., Spence, P., and Heywood, K. J.: The Antarctic Slope Current in a Changing Climate, Reviews of Geophysics,

595 56, 741–770, https://doi.org/https://doi.org/10.1029/2018RG000624, 2018.

Verfaillie, D., Pelletier, C., Goosse, H., Jourdain, N. C., Bull, C. Y. S., Dalaiden, Q., Favier, V., Fichefet, T., and Wille, J. D.: The circum-Antarctic ice-shelves respond to a more positive Southern Annular Mode with regionally varied melting, COMMUNICATIONS EARTH & ENVIRONMENT, 3, https://doi.org/10.1038/s43247-022-00458-x, 2022.

Wang, Y., Zhao, C., Gladstone, R., Galton-Fenzi, B., and Warner, R.: Thermal structure of the Amery Ice Shelf from borehole observations

600 and simulations, The Cryosphere, 16, 1221–1245, https://doi.org/10.5194/tc-16-1221-2022, 2022.

Wells, A. J. and Worster, M. G.: A geophysical-scale model of vertical natural convection boundary layers, Journal of Fluid Mechanics, 609, 111–137, https://doi.org/10.1017/S0022112008002346, 2008.

Wen, J., Wang, Y., Wang, W., Jezek, K., Liu, H., and Allison, I.: Basal melting and freezing under the Amery Ice Shelf, East Antarctica, Journal of Glaciology, 56, 81–90, https://doi.org/10.3189/002214310791190820, 2010.

605 Williams, G. D., Herraiz-Borreguero, L., Roquet, F., Tamura, T., Ohshima, K. I., Fukamachi, Y., Fraser, A. D., Gao, L., Chen, H., McMahon, C. R., Harcourt, R., and Hindell, M.: The suppression of Antarctic bottom water formation by melting ice shelves in Prydz Bay, NATURE COMMUNICATIONS, 7, https://doi.org/10.1038/ncomms12577, 2016.

Xu, Y., Rignot, E., Fenty, I., Menemenlis, D., and Flexas, M. M.: Subaqueous melting of Store Glacier, west Greenland from three-dimensional, high-resolution numerical modeling and ocean observations, Geophysical Research Letters, 40, 4648–4653,

610 https://doi.org/https://doi.org/10.1002/grl.50825, 2013.

Yang, J., Guo, J., Greenbaum, J. S., Cui, X., Tu, L., Li, L., Jong, L. M., Tang, X., Li, B., Blankenship, D. D., Roberts, J. L., van Ommen, T., and Sun, B.: Bathymetry Beneath the Amery Ice Shelf, East Antarctica, Revealed by Airborne Gravity, Geophysical Research Letters, 48, e2021GL096 215, https://doi.org/https://doi.org/10.1029/2021GL096215, e2021GL096215 2021GL096215, 2021.

Yu, J., Liu, H., Jezek, K. C., Warner, R. C., and Wen, J.: Analysis of velocity field, mass balance, and basal melt of the Lambert Glacier–Amery

615 Ice Shelf system by incorporating Radarsat SAR interferometry and ICESat laser altimetry measurements, Journal of Geophysical Research: Solid Earth, 115, https://doi.org/https://doi.org/10.1029/2010JB007456, 2010.